Hydrodynamic Model Description

Macleans Nose, Sound of Mull

CAR/L/1002965/V7

May 2022

[redacted]

CONTENTS

LIST OF FIGURES

LIST OF TABLES

1. Model Description

The hydrodynamic model used in the Macleans Nose solids waste deposition modelling report (Mowi Scotland Ltd., 2022) was RiCOM (River and Coastal Ocean Model), a general-purpose hydrodynamics and transport model, which solves the standard Reynolds-averaged Navier-Stokes equation (RANS) and the incompressibility condition, applying the hydrostatic and Boussinesq approximations. It has been tested on a variety of benchmarks against both analytical and experimental data sets (e.g. Walters & Casulli 1998; Walters 2005a, b). The model has been previously used to investigate the inundation risk from tsunamis and storm surge on the New Zealand coastline (Walters 2005a; Gillibrand et al. 2011; Lane et al. 2011), to study tidal currents in high energy tidal environments (Walters et al. 2010) and, more recently, to study tidal energy resource (Plew & Stevens 2013; Walters et al. 2013; Walters 2016) and the effects of energy extraction on the ambient environment (McIlvenny et al. 2016; Gillibrand et al. 2016).

The basic equations considered here are the three-dimensional (3D) shallow water equations, derived from the Reynolds-averaged Navier-Stokes equations by using the hydrostatic assumption and the Boussinesq approximation. The continuity equation for incompressible flows is:

$$\nabla \cdot u + \frac{\partial w}{\partial z} = 0 \tag{1}$$

where **u**(x,y,z,t) is the horizontal velocity vector, w(x,y,z,t) is the vertical velocity, ∇ is the horizontal gradient operator, and z is the vertical coordinate. The momentum equation in non-conservative form is given by:

$$\frac{Du}{Dt} + f\hat{z} \times u + \frac{1}{\rho_0}\nabla p - \frac{\partial}{\partial z}\left(A_V \frac{\partial u}{\partial z}\right) - \nabla \cdot (A_h \nabla u) + F = 0 \tag{2}$$

where t is time; f(x,y) is the Coriolis parameter; $\hat{z}$ is the upward unit vector; p(x,y,z,t) is pressure; ρ_0 is a reference density; A_V(x,y,z,t) and A_h(x,y,z,t) are the vertical and horizontal eddy viscosities respectively; **F** represents body forces including form drag from obstacles in the flow; and x, y are the horizontal coordinates aligned to the east and north respectively.

The free surface equation is formed by vertically integrating the continuity equation and applying the kinematic free surface and bottom boundary conditions:

$$\frac{\partial \eta}{\partial t} - \nabla \cdot \left(\int_{-H}^{\eta} u dz\right) = 0 \tag{3}$$

where H is the water depth relative to the mean level of the sea.

The model can be run in two- or three-dimensional mode. Frictional stress, $\boldsymbol{\tau}_b$, is applied at the seabed as a quadratic function of velocity:

$$\tau_b = \rho C_D U_b |U_b| \tag{4}$$

where ρ = 1025 kg m^{-3} is the water density. The velocity, U_b, is either the velocity at the lowest sigma layer if the model is run in 3D or the depth-averaged velocity if run in 2D. The drag coefficient, C_D, can be either a constant or calculated from the bed roughness lengthscale, z_0, using:

$$C_D = \left(\frac{\kappa}{\ln\left((z_b+z_0)/z_0\right)}\right)^2 \quad (5)$$

where κ=0.4 is von Karman's constant, and z_b is the height above the bed of the lowest velocity point.

Wind forcing was applied as a surface stress calculated from hourly wind speed and direction. Wind stress was calculated from the wind velocity by a standard quadratic relation:

$$\tau_x = \rho_a C_S u W \quad (6a)$$
$$\tau_y = \rho_a C_S v W \quad (6b)$$

where (u,v) are the East and North components of wind velocity respectively, W is the wind speed ($W = [u^2+v^2]^{½}$), ρ_a is the density of air, and the surface drag coefficient C_S is calculated following Wu (1982) or Large and Pond (1981).

The equations are discretized on an unstructured grid of triangular elements which permits greater resolution of complex coastlines. The momentum and free surface equations are solved using semi-implicit techniques to optimize solution time and avoid the CFL stability constraint (Walters 2016). The material derivative in (2) is discretized using semi-Lagrangian methods to remove stability constraints on advection (Casulli, 1987; Walters et al. 2008). The Coriolis term is solved using a 3rd order Adams-Bashforth method (Walters et al. 2009). Full details of the model discretization and solution methods can be found in Walters et al. (2013) and Walters (2016). The solution methods provide a fast, accurate and robust code that runs efficiently on multi-core desktop workstations with shared memory using OpenMP. Full details of the model discretization and solution methods, including the basis of the application to tidal energy, are given by Walters et al. (2013) and Walters (2016).

2. Configuration and Boundary Forcing for Macleans Nose

The unstructured mesh used in the model was adapted from the Wider Loch Linnhe System (WLLS) sub-model mesh of the Scottish Shelf Model (SSM; Marine Scotland, 2016). In the adapted mesh, the Sound of Raasay and waters to the north of Kyle Rhea have been removed, since these were causing instability in the model and do not contribute significantly to the oceanography of the region to the south of Skye. The modified domain and mesh is shown in Figure 1, with the area around Macleans Nose shown in Figure 2.

The mesh was refined in the area around the Macleans Nose site (Figure 3). The spatial resolution of the model varied from 22m in some inshore waters to 7.8 km along the open boundary. In total, the model consisted of 112,339 nodes and 211,949 triangular elements.

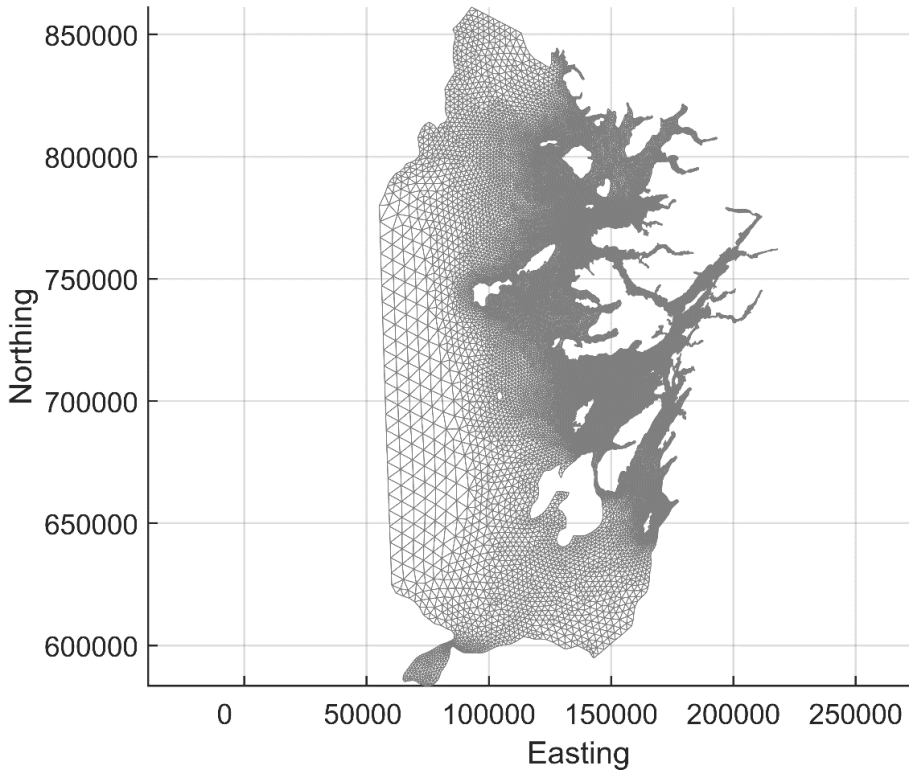

Figure 1. The modified WLLS domain and mesh used in the Macleans Nose modelling.

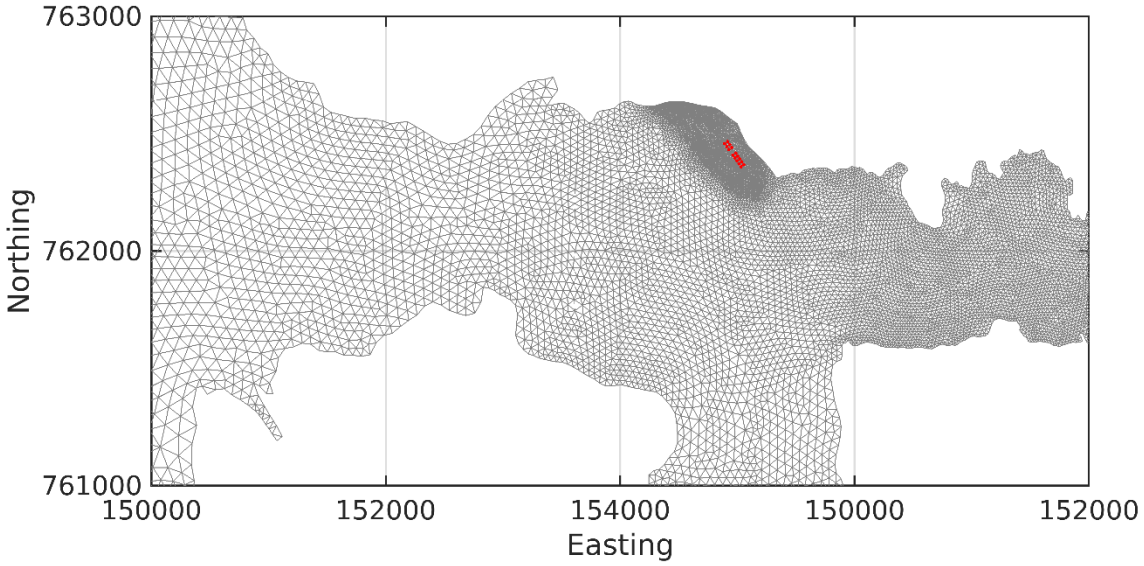

Figure 2. The unstructured mesh around the Macleans Nose site in Outer Loch Sunart and the Sound of Mull. The pen locations are indicated (•).

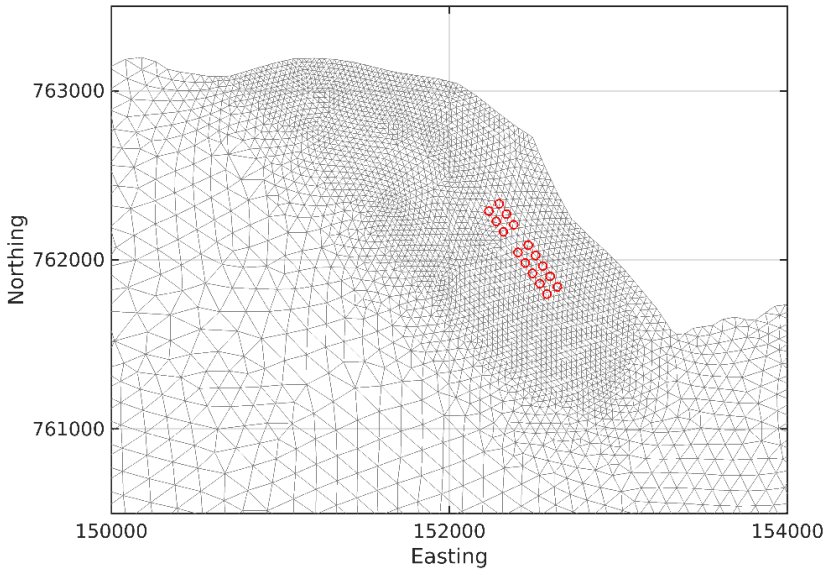

Figure 3. The unstructured mesh around the Macleans Nose site. The pen locations are indicated (o).

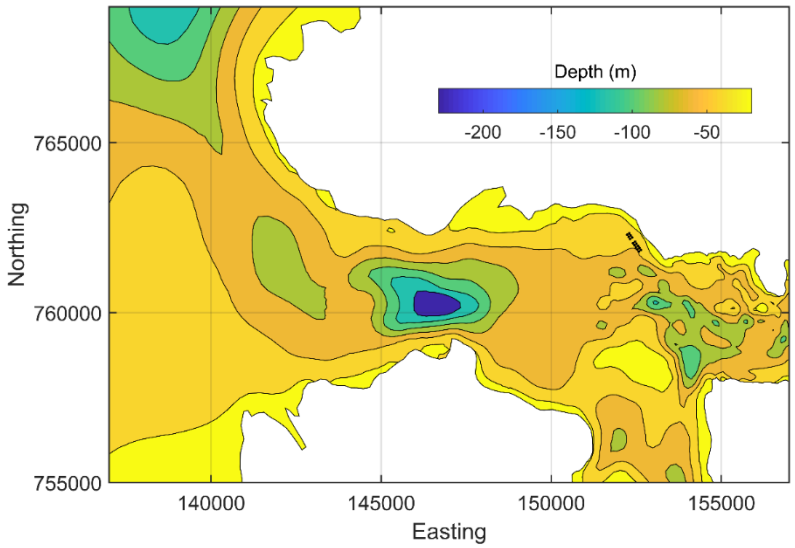

Figure 4. Model water depths, H (m), in the area around the Macleans Nose farm. The cage locations are indicated (•).

The model was forced along its open boundary by eight tidal constituents (O_1, K_1, Q_1, P_1, M_2, S_2, N_2, K_2), amplitudes and phase of which were obtained from the full Scottish Shelf Model. Spatially- and temporally-varying wind speed and direction data were taken from the ERA5 global reanalysis dataset for the required simulation periods (ECMWF, 2021), with the data converted to surface stress using Equation 6.

The model was run in 3D mode with 10 sigma layers evenly distributed over the water depth. Climatological river flow data, taken from the WLLS climatological runs (Marine Scotland, 2016) were used. In all, 134 rivers are included in the WLLS domain, with nine entering the

domain in Loch Sunart and the western Sound of Mull. The climatological seasonal cycles of daily river flows in these nine rivers are shown in Figure 5.

In the vertical, a general length-scale (gls) turbulence closure scheme was used (Umlauf and Burchard, 2003; Warner et al., 2005). The closure scheme requires bed and surface roughness lengthscales to be specified; these parameters were refined during the calibration process.

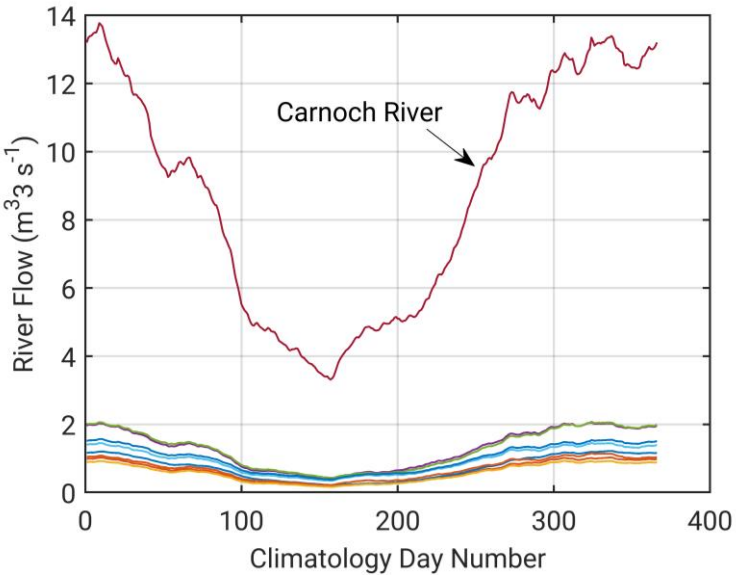

Figure 5. Averaged flows from 9 rivers and streams entering Loch Sunart and the western Sound of Mull from the 30-year climatology used by the Scottish Shelf Model. The largest flow is from the Carnoch River at the head of Loch Sunart.

3. Model Calibration and Validation

The RiCOM model has previously been calibrated against sea level and current meter data from the north of Scotland (Gillibrand et al. 2016). For the current study, the model was further calibrated against hydrographic data collected at the site in 2017 (Figure 6). Data are available from:

- 22nd March – 4th May 2017 (ID152, Macleans Nose North)
- 5th May – 3rd July 2017 (ID159 and ID160, Macleans Nose North and South).

In total, the data extend over 102 days. Two ADCPs were deployed on both occasions (Figure 6), but the southern deployment during March – May 2017 (ID153) was corrupted and was not used for calibration/validation. Calibration was performed in a standard fashion, with bed friction and diffusion/dispersion coefficients adjusted to obtain the best fit against the observed sea surface height and current data. For the present location, stratification was considered to be significant and the model was run in 3D mode. The model was spun up for three days, and then run for the same periods as the observations and the modelled tidal elevation and velocity at the site evaluated against the observed data. Boundary temperature and salinity, and river flow data, were taken from the 30-year climatology produced by the Scottish Shelf Model (Marine Scotland, 2016b), corresponding to the time of year of the observations (March – July).

The calibrated modelled elevation and velocity are presented alongside the observed data below.

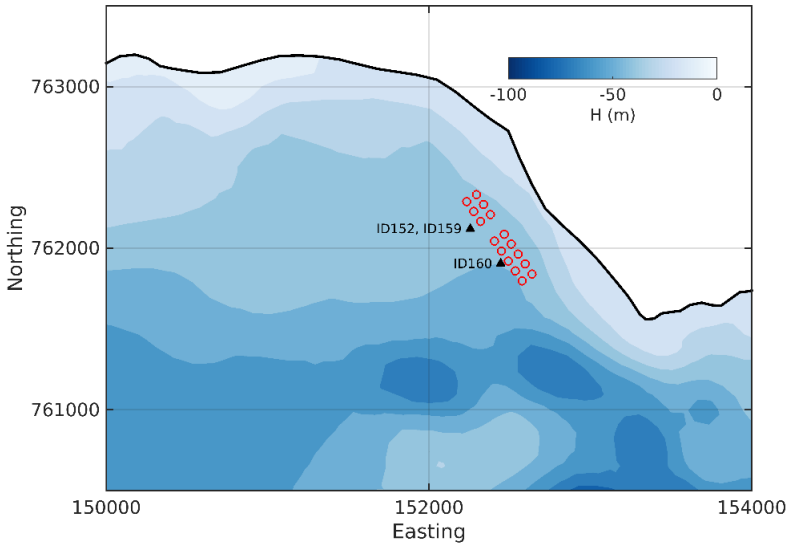

Figure 6. Locations of the ADCP deployments (▲) relative to the pens (o) at Macleans Nose. Water depths (H, m) are shaded.

Model performance was assessed using three metrics: the mean absolute error (MAE), the root-mean-square error (RMSE) and the model skill (d_2). The first two are standard measures of model accuracy; the third, d_2, is taken from Willmott et al. (1985) and lies in the range $0 \leq d_2 \leq 1$, with $d_2 = 0$ implying zero model skill and $d_2 = 1$ indicating perfect skill.

3.1 Calibration: 22nd March – 4th May 2017 (ID152)

The calibration used observed depth and current velocity from the ADCP location to compare with modelled sea surface height (SSH) and velocity (ADCP deployment ID152). The model was calibrated by varying the value of the bed and surface roughness lengthscales, z_0 and z_s. Simulations were performed with a range of values of both parameters, varying over the range $0.001 \leq z_0, z_s \leq 1.0$. After a number of simulations, a final parameter set was selected (Table 1).

The results of the calibration exercise are presented in Figure 7 – Figure 11 and Table 2. At the ADCP location, the sea surface height was accurately modelled, with model skill of 0.99. The mean absolute error (MAE) and root-mean-square error (RMSE) values of 0.14 m and 0.17 respectively are about 2.8% and 3.4% of the spring tide range respectively.

Table 1. Parameter values chosen for the RiCOM model from the calibration simulations.

Parameter Description	Value
Bed roughness lengthscale, z_0 (m)	0.03
Surface roughness lengthscale, z_s (m)	0.1
Number of vertical layers	10
Model time step (s)	36.0

For the calibration period, the model skill scores were 0.43 and 0.45 for the East and North components of near-surface (7.8m) velocity respectively, with RMSE values of 0.07 m s^{-1} and 0.08 m s^{-1} for the two components of velocity (Table 2). At mid-depth of 16.8 m, the skill scores were 0.40 and 0.42 respectively, with RMSE in the range 0.05 – 0.07. At the near-bed depth, the skill are were lower, with RMSE in the range 0.04 – 0.07.

These skill scores are lower than usually considered acceptable due to the complex baroclinic dynamics evident in the observations at the site (Figure 8). Internal waves are known to propagate in Loch Sunart (Elliott et al., 1992) and the data exhibit signals of significant internal wave activity at Macleans Nose, the strength of which is strongly dependent on the strength of stratification at the site during the observation period. Because we used climatological river runoff, rather than measured data, to force the model (due to a lack of accurate river flow data for the area, and a wish to have more generic rather than time-specific results), the simulated stratification almost certainly differed from the actual stratification, leading to differences in the simulated and observed baroclinic dynamics. These differences are manifest as differences in the tidal phase between observed and modelled velocity (Figure 9). Even though the magnitude of the current is well simulated, the phase lag between model and data leads to an enhanced error metrics. Note that the phase of the sea surface height is accurately reproduced (Figure 7), so we are confident that the barotropic tide is well simulated.

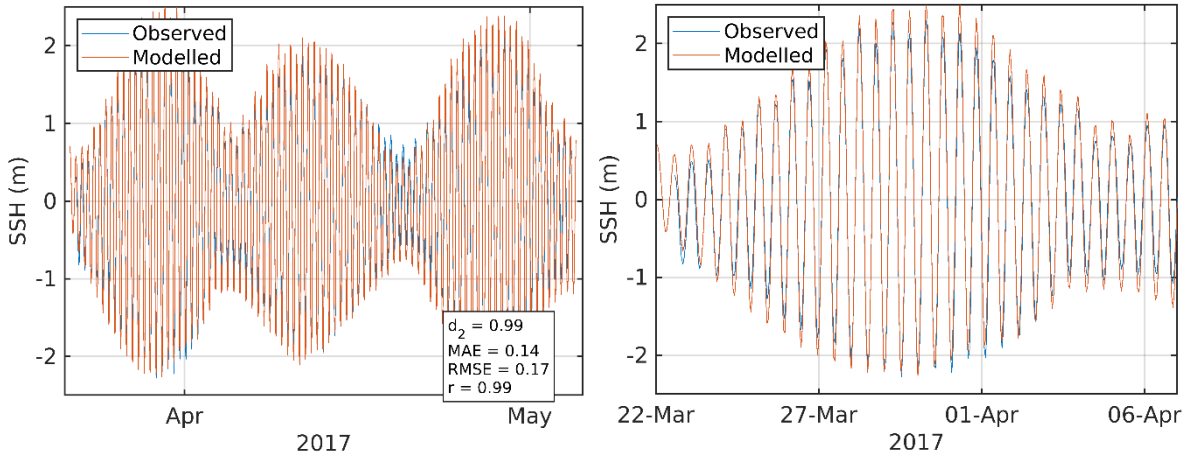

Figure 7. Comparison between observed and modelled sea surface height from March - May 2017 (ADCP deployment ID152) using model parameter values from Table 1. Both the full record (left) and a subset of 15 days (right) are shown. Observed data are in blue, model results in red.

Table 2. Model performance statistics for sea surface height (SSH) and East and North velocity at the ADCP location ID152 from December 2016 – February 2017 at three depths: 7.8m, 16.8m and 36.8m.

		Skill, d_2	MAE	RMSE
Sea Surface Height (SSH, m)		0.99	0.14	0.17
7.8 m	East Velocity (m s^{-1})	0.43	0.05	0.07
	North Velocity (m s^{-1})	0.45	0.07	0.08
16.8 m	East Velocity (m s^{-1})	0.40	0.05	0.06
	North Velocity (m s^{-1})	0.42	0.05	0.07
36.8 m	East Velocity (m s^{-1})	0.26	0.04	0.05
	North Velocity (m s^{-1})	0.19	0.06	0.07

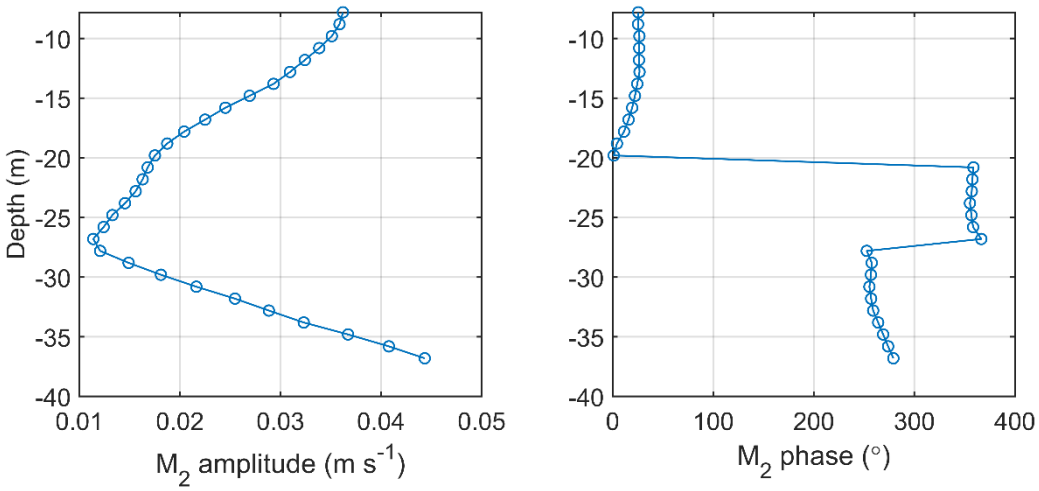

Figure 8. Observed semi-major axis amplitude (left) and phase (right) of the M_2 tidal constituent at Macleans Nose during March – May 2017 (ID152). The mid-depth changes in both amplitude and phase are strongly indicative of baroclinic wave activity. The tidal analysis was performed in Matlab using T_TIDE (Pawlowicz et al., 2002).

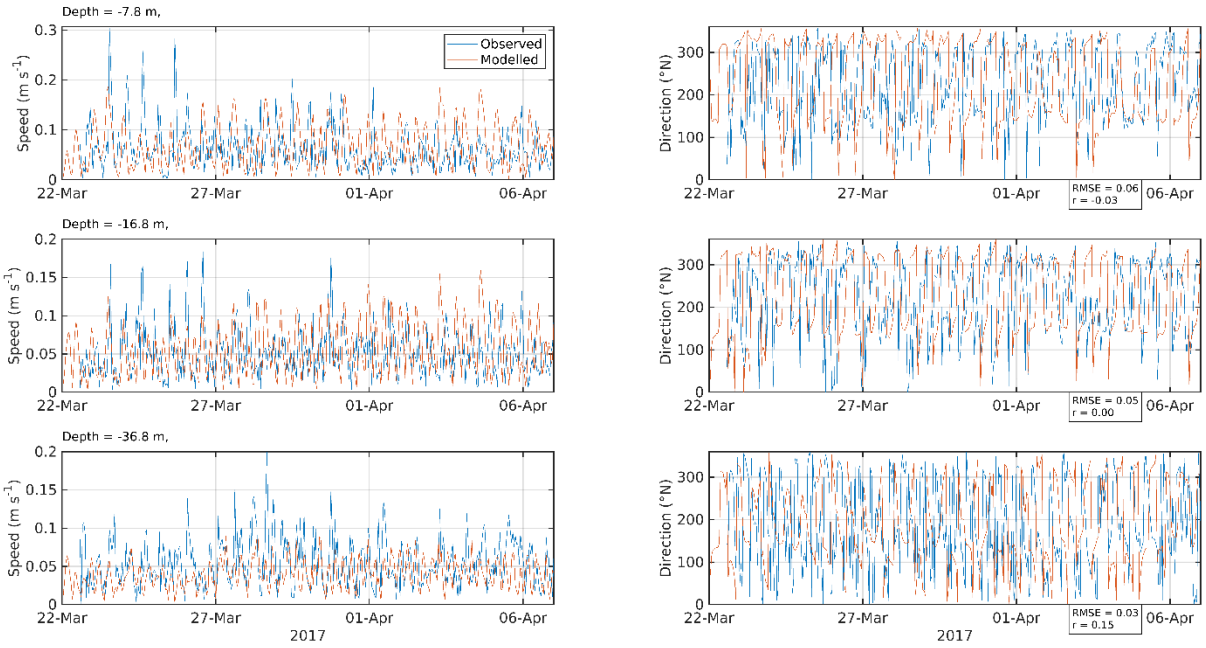

Figure 9. Comparison between observed and modelled East (left) and North (right) components of velocity at the ADCP location for 15 days in March – April 2017 (ID152) at three depths: 7.8 m (top), 16.8 m (middle) and 36.8 m (bottom). Observed data are in blue, model results in red.

The scatter plots (Figure 10) and histograms (Figure 11) demonstrate that despite the phase difference between modelled and observed velocity, the magnitude and direction of the

modelled currents compare very well with observations. As a result, simulations of waste deposition should not be adversely affected by the velocity phase difference (which will be variable anyway).

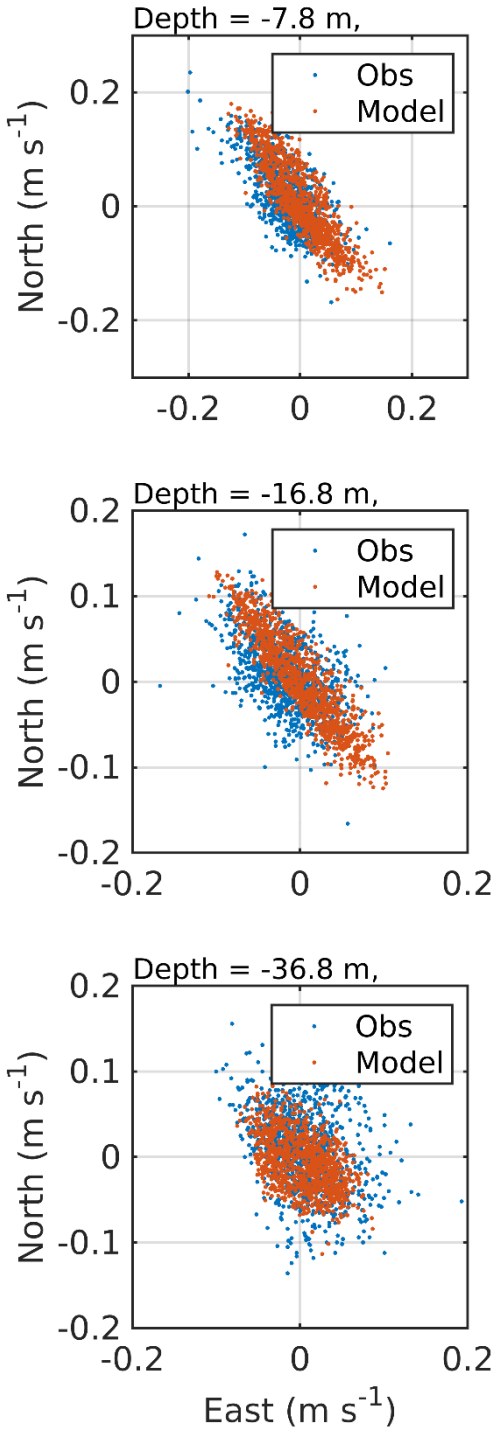

Figure 10. Scatter plot of observed and modelled velocity at the ADCP location from March – May 2017 (ID152) at three depths: 7.8 m (top), 16.8 m (middle) and 36.8 m (bottom). Observed data are in blue, model results in red.

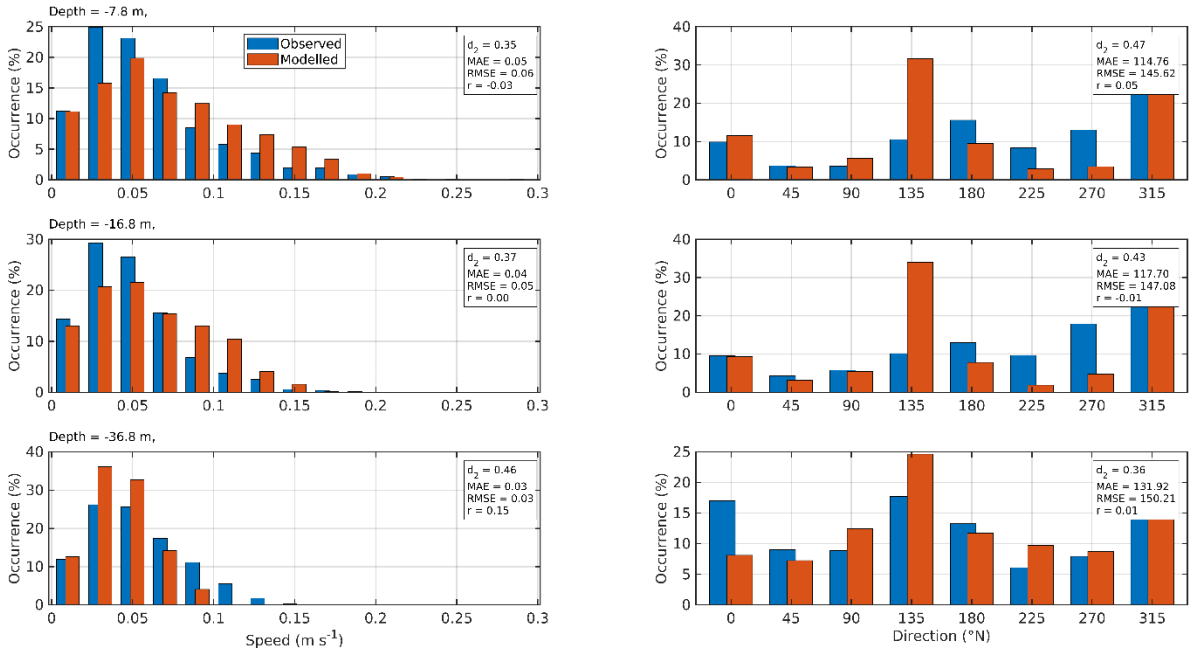

Figure 11. Histograms of observed and modelled speed (left) and direction (right) at the ADCP location from March – May 2017 (ID152) at three depths: 7.8 m (top), 17.8 m (middle) and 36.8 m (bottom). Observed data are in blue, model results in red.

3.2 Validation: 5th May – 3rd July 2017 (ID159)

At the ADCP location, the sea surface height was reasonably modelled, with model skill of 0.99 (Figure 12, Table 3). The mean absolute error (MAE) and root-mean-square error (RMSE) values of 0.18 m and 0.23 respectively are about 3.6% and 4.6% of the spring tide range respectively.

Table 3. Model performance statistics for sea surface height (SSH), and East and North velocity at the ADCP location from May – July 2017 (ID159) at three depths, 7.2m 16.2 m and 36.2 m.

		Skill, d_2	MAE	RMSE
Sea Surface Height (SSH, m)		0.99	0.18	0.23
7.2m	East Velocity (m s^{-1})	0.52	0.05	0.06
	North Velocity (m s^{-1})	0.58	0.05	0.07
16.2m	East Velocity (m s^{-1})	0.46	0.05	0.06
	North Velocity (m s^{-1})	0.49	0.05	0.06
36.2m	East Velocity (m s^{-1})	0.32	0.04	0.05
	North Velocity (m s^{-1})	0.27	0.04	0.06

Model skill scores were 0.52 and 0.58 for the East and North components of near-surface (7.2 m) velocity respectively, with RMSE values of 0.06 m s^{-1} and 0.07 m s^{-1} respectively. (Figure 13, Table 3). As with the calibration simulation (ID152) the phase of the modelled velocity

differed, sometimes significantly, from the observed velocity phase. However, the scatter plots and (Figure 14) histograms (Figure 15) demonstrate again that the magnitude and direction of the observed currents were well simulated by the model.

At mid- and near-bed depths, the RMSE values were similar to those at the surface (0.04 – 0.06 m s^{-1}). The difference in phase between model and data was particularly enhanced at the near-bed depth, leading to lower skill scores (0.32 and 0.27 for East and North components respectively), although the scatter plots (Figure 14) and histograms (Figure 15) demonstrate the accurate prediction of current magnitude and direction at the seabed.

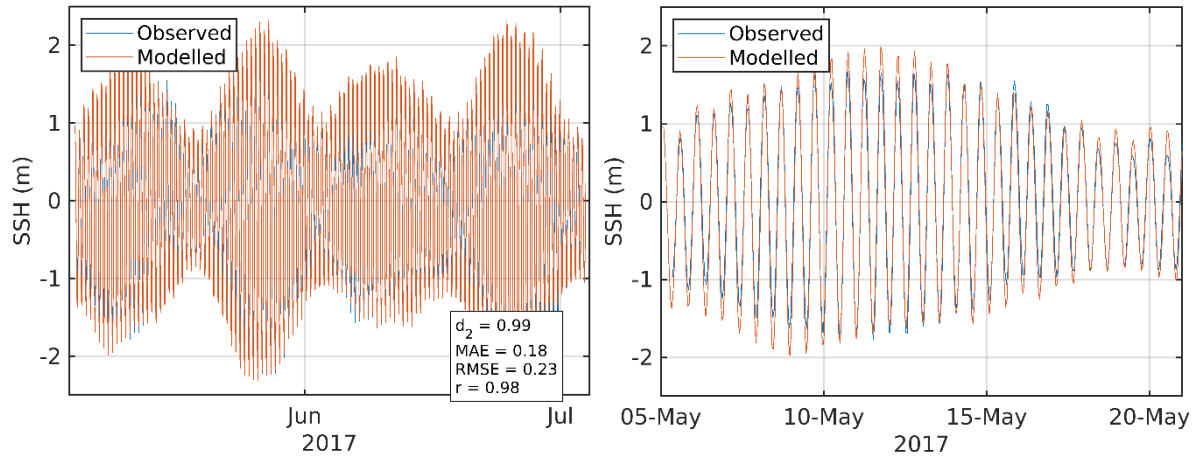

Figure 12. Comparison between observed and modelled sea surface height from May – July 2017 (ADCP deployment ID159) using model parameter values from Table 1. Both the full record (left) and a subset of 15 days (right) are shown. Observed data are in blue, model results in red.

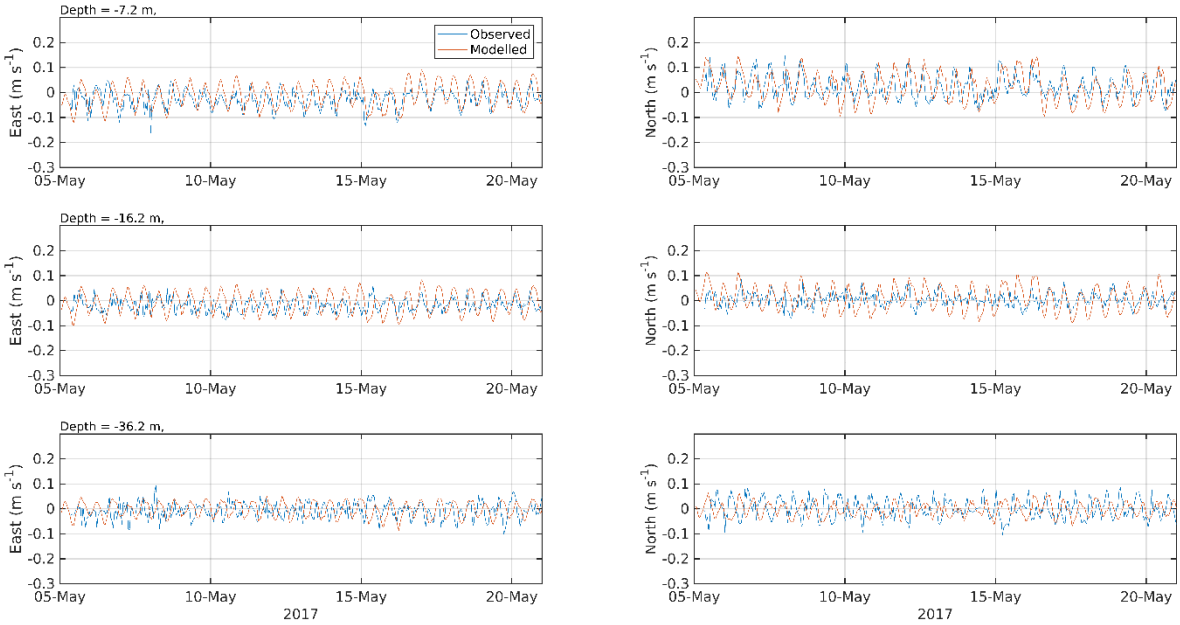

Figure 13. Comparison between observed and modelled East (left) and North (right) components of velocity at the ADCP location for 15 days in May 2017 (ID159) at three depths: 7.2 m (top), 16.2 m (middle) and 36.2 m (bottom). Observed data are in blue, model results in red.

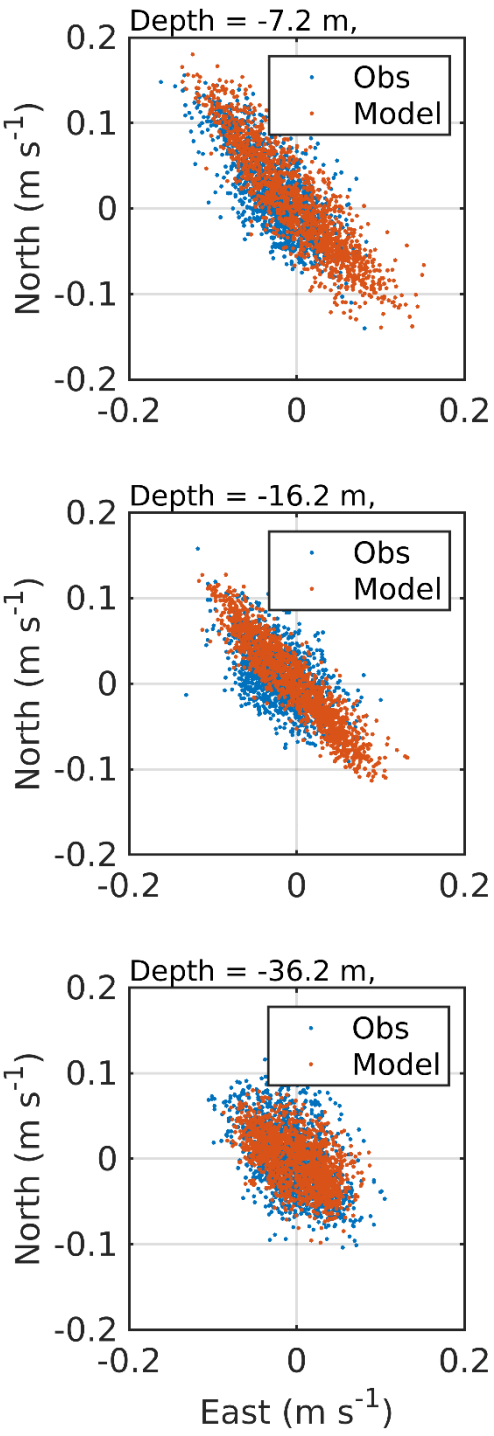

Figure 14. Scatter plot of observed and modelled velocity at the ADCP location from May – July 2017 (ID159) at three depths: 7.2 m (top), 16.2 m (middle) and 36.2 m (bottom). Observed data are in blue, model results in red.

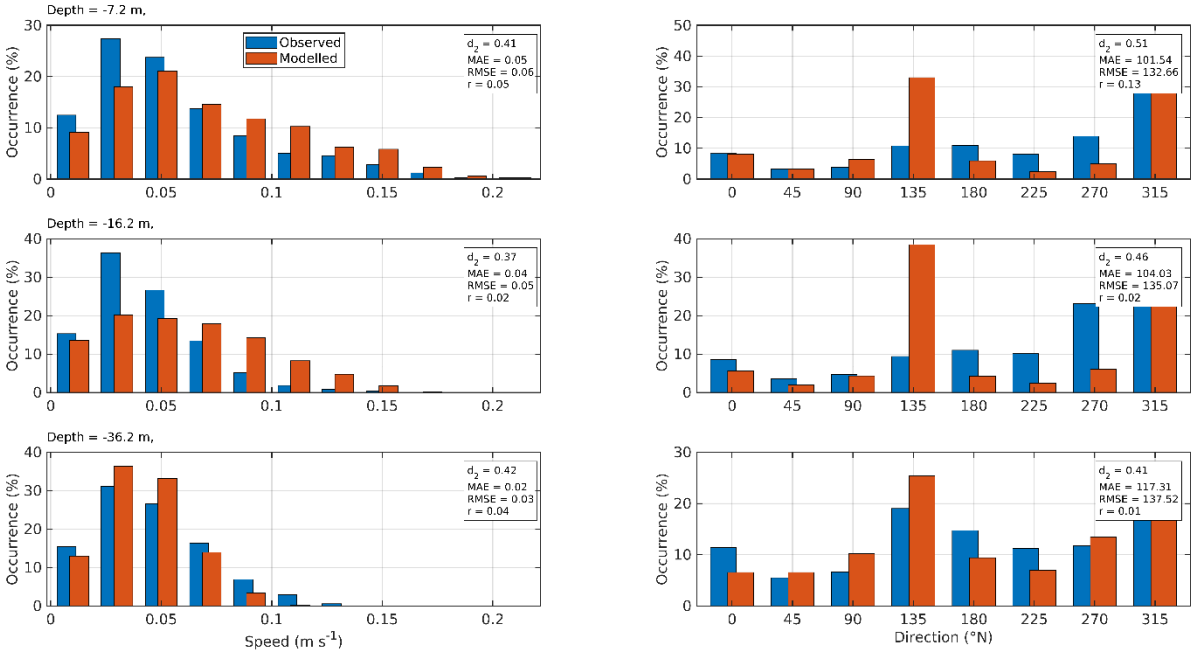

Figure 15. Histograms of observed and modelled current speed (left) and direction (right) at the ADCP location from May – July 2017 (ID159) at three depths: 7.2 m (top), 16.2 m (middle) and 36.2 m (bottom). Observed data are in blue, model results in red.

3.3 Validation: 5th May – 3rd July 2017 (ID160)

At the ADCP location, the sea surface height was reasonably modelled, with model skill of 0.99 (Figure 16, Table 4). The mean absolute error (MAE) and root-mean-square error (RMSE) values of 0.20 m and 0.25 are 4% and 5% respectively of the spring tide range.

Table 4. Model performance statistics for sea surface height (SSH), and East and North velocity at the ADCP location from May – July 2017 (ID160) at three depths: 7.8m 16.8 m and 42.8 m.

		Skill, d_2	MAE	RMSE
Sea Surface Height (SSH, m)		0.99	0.20	0.25
7.8 m	East Velocity (m s^{-1})	0.46	0.05	0.07
	North Velocity (m s^{-1})	0.58	0.06	0.07
16.8 m	East Velocity (m s^{-1})	0.53	0.05	0.06
	North Velocity (m s^{-1})	0.55	0.05	0.06
42.8m	East Velocity (m s^{-1})	0.50	0.03	0.04
	North Velocity (m s^{-1})	0.20	0.06	0.07

East and north components of near-surface (7.8 m depth) velocity at the ADCP location were satisfactorily reproduced by the model, with values of the model skill, d_2, of 0.46 and 0.58 respectively (Figure 17, Table 4). The values of the MAE and RMSE were in the range 0.05 – 0.07 m s^{-1} (Table 4). At mid-depth (16.8 m), the model skill, RMSE and MAE values were

similar. The scatter plots and histograms shown in Figure 18 and Figure 19 demonstrate that the modelled currents were broadly of the same speed and direction as the observed data.

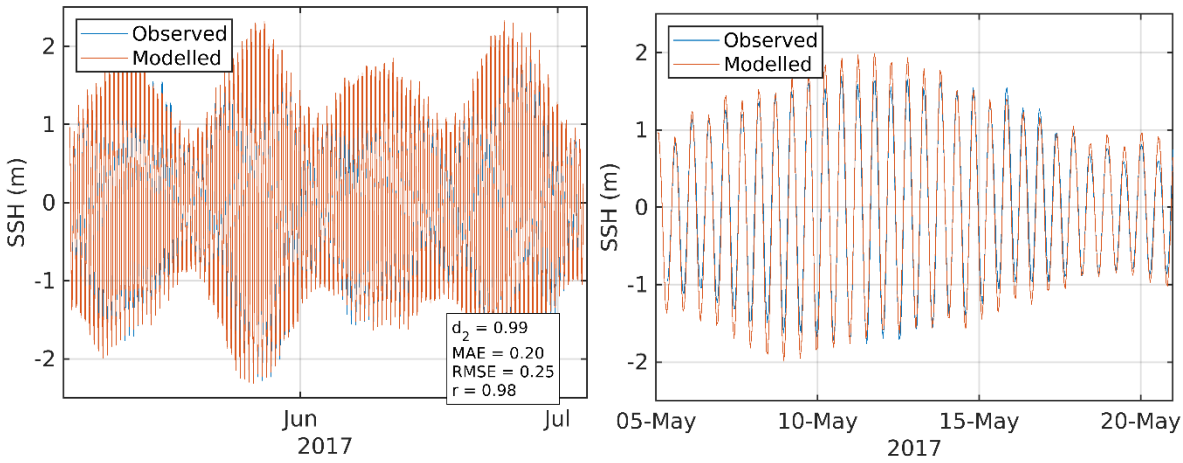

Figure 16. Comparison between observed and modelled sea surface height from May – July 2017 (ADCP deployment ID160) using model parameter values from Table 1. Both the full record (left) and a subset of 15 days (right) are shown. Observed data are in blue, model results in red.

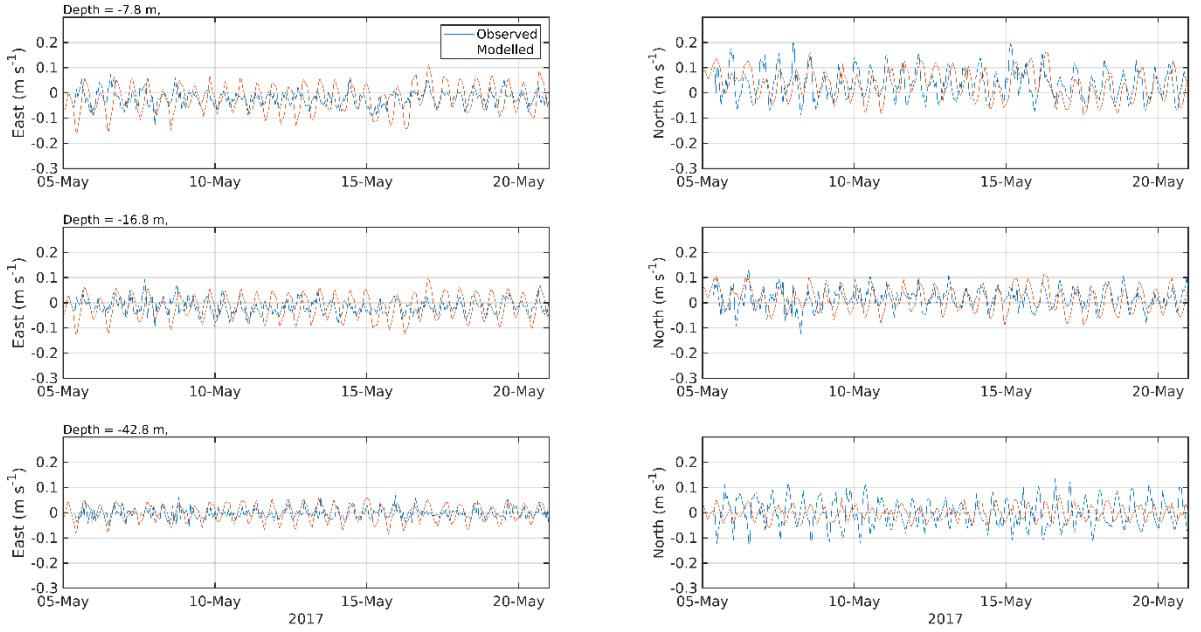

Figure 17. Comparison between observed and modelled East (left) and North (right) components of velocity at the ADCP location for 15 days in May 2017 (ID160) at three depths: 7.8 m (top), 16.8 m (middle) and 42.8 m (bottom). Observed data are in blue, model results in red.

The observed near-bed velocity data at 42.8m exhibit a curious feature (Figure 18). The orientation of the near-bed flow is to the NNE, rather than the NW like the near-surface and mid-depth flow. Despite numerous attempts, we have been unable to reproduce the observed

orientation in the model results. The modelled velocities are orientated to the NW, similar to those at the shallower depths. We suspect that a small-scale bathymetric feature close to the deployment location, not resolved in the model bathymetry, is steering the near-bed flow in a direction offset from the main flow.

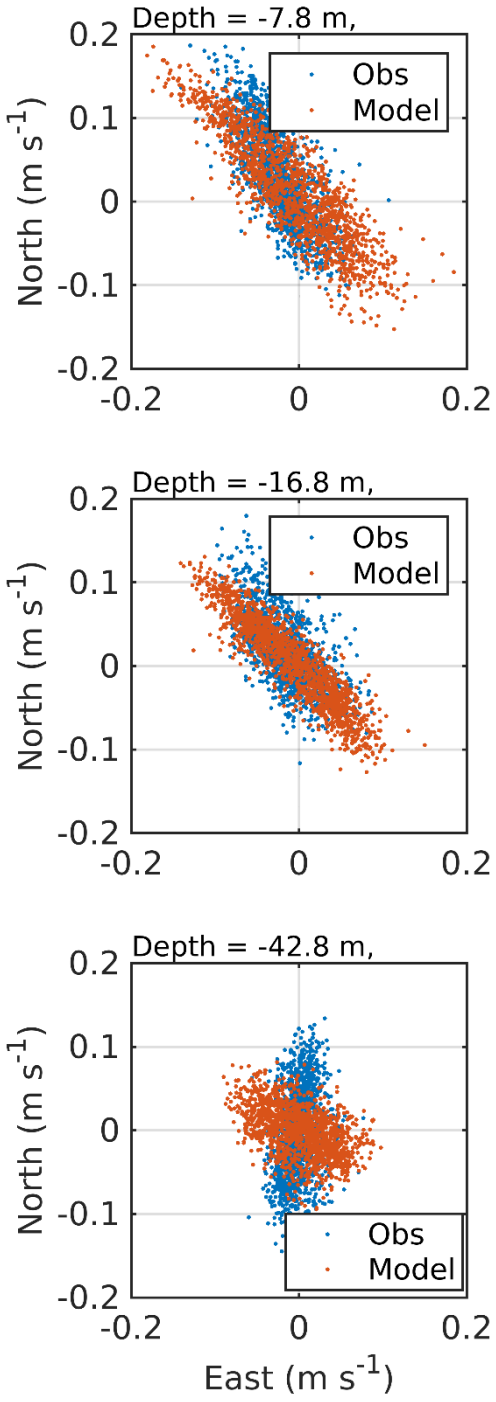

Figure 18. Scatter plot of observed and modelled velocity at the ADCP location from May – July 2017 (ID160) at three depths: 7.8m (top), 16.8 m (middle) and 42.8m (bottom). Observed data are in blue, model results in red.

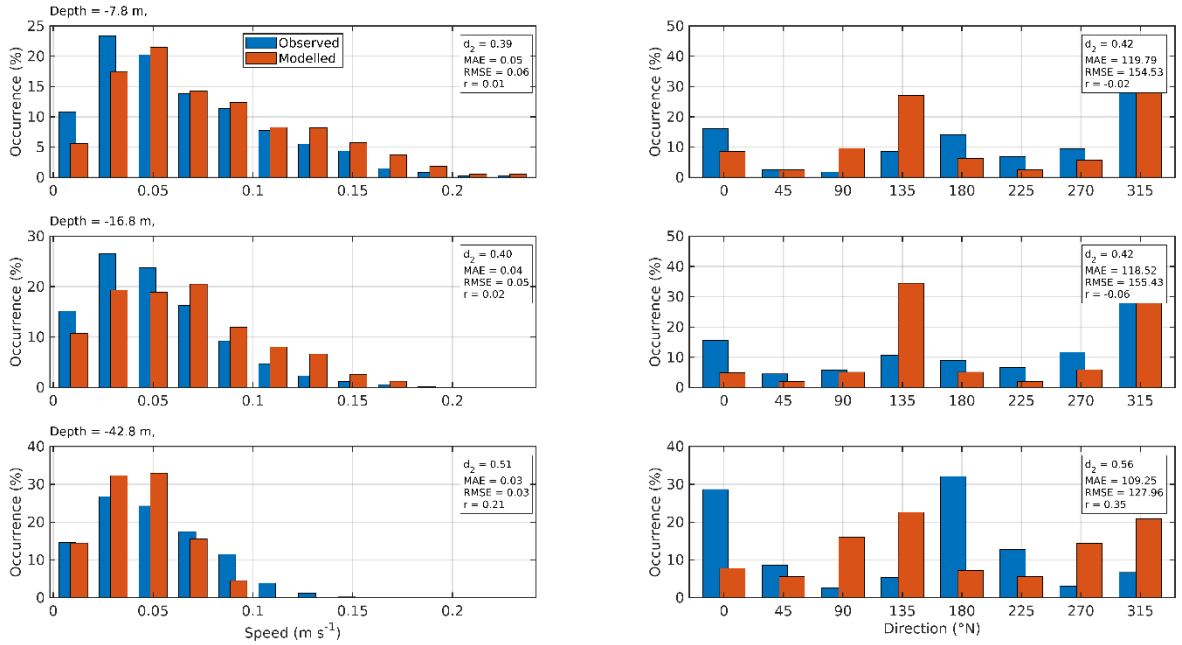

Figure 19. Histograms of observed and modelled current speed (left) and direction (right) at the ADCP location from May – July 2017 (ID160) at three depths: 7.8m (top), 16.8 m (middle) and 42.8m (bottom). Observed data are in blue, model results in red.

4. Modelled Flow Fields

Modelled near-surface flood and ebb velocity vectors at spring tides are illustrated in Figure 20. Modelled current speeds in the Sound of Mull at springs were typically 20 cm s^{-1}, but currents were weaker flowing around the Macleans Nose site. Modelled currents speeds were weaker during neap tides (Figure 21), although not substantially in the case shown. Near-surface currents are, of course, affected by wind forcing and baroclinic dynamics as well as tidal forcing.

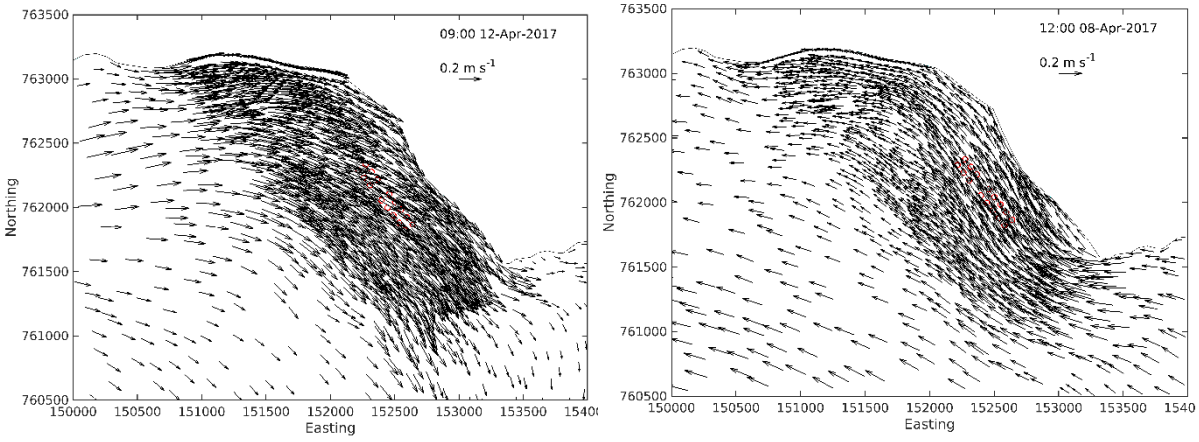

Figure 20. Modelled flood (left) and ebb (right) surface current vectors during spring tides on 12th April and 8th April 2017 respectively. For clarity, only 25% of the model vectors are shown. The locations of the farm pens are indicated (O).

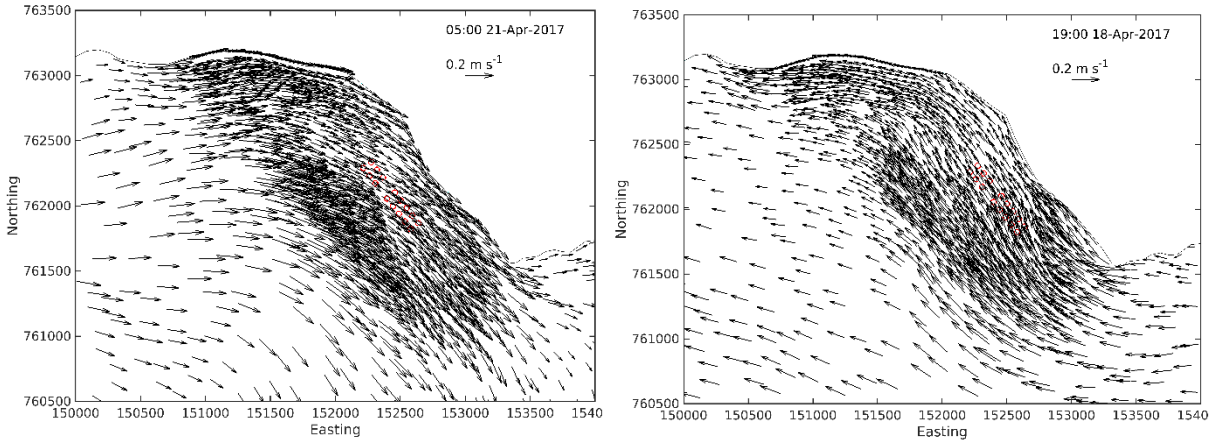

Figure 21. Modelled flood (left) and ebb (right) surface current vectors during neap tides on 21st April and 18th April 2017 respectively. For clarity, only 25% of the model vectors are shown. The locations of the farm pens are indicated (O).

5. Modelled Velocity, January – April 2020

For the NewDepomod simulations, RiCOM was run from 29th January – 28th April 2020 (90 days) using the same parameter set described in this report (Table 1). Wind forcing was again taken from ERA5 (ECMWF, 2021) and climatological river flows used. The modelled near-bed East and North components of velocity for this period, at both ADCP deployment locations, are shown in Figure 22. Note that although the modelled velocities are shown for the ADCP locations, current measurements were not made at the site in 2020; these model results are shown for indirect comparison with previous simulations and data only.

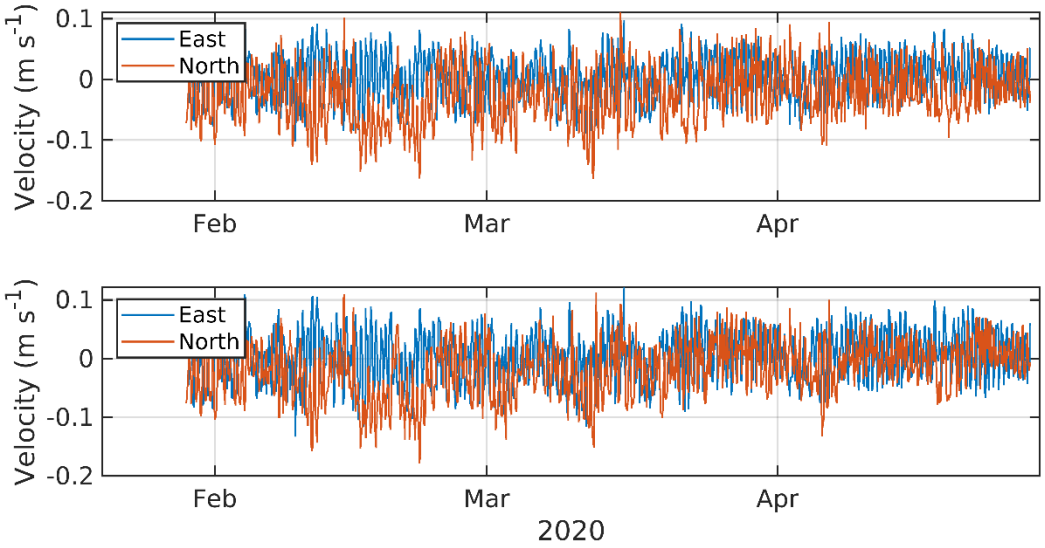

Figure 22. Modelled near-bed East and North components of velocity at the northern (top) and southern (bottom) ADCP locations for the period January – April 2020. Observations of velocity were not made at this time, so the modelled results cannot be compared directly with data.

The modelled near-bed velocity results from 2020 are compared with the measured data from 2017 (ID152 and ID160) as a scatter plot (Figure 23). These results are shown to demonstrate that the flow fields used with NewDepomod in the waste solids dispersion modelling (Mowi, 2022) are consistent in direction and magnitude with the model results from the calibration process described in this report (e.g. Figure 10 and Figure 18). Note that the (localised) difference in near-bed current direction between model and data is still evident at the ID160 location.

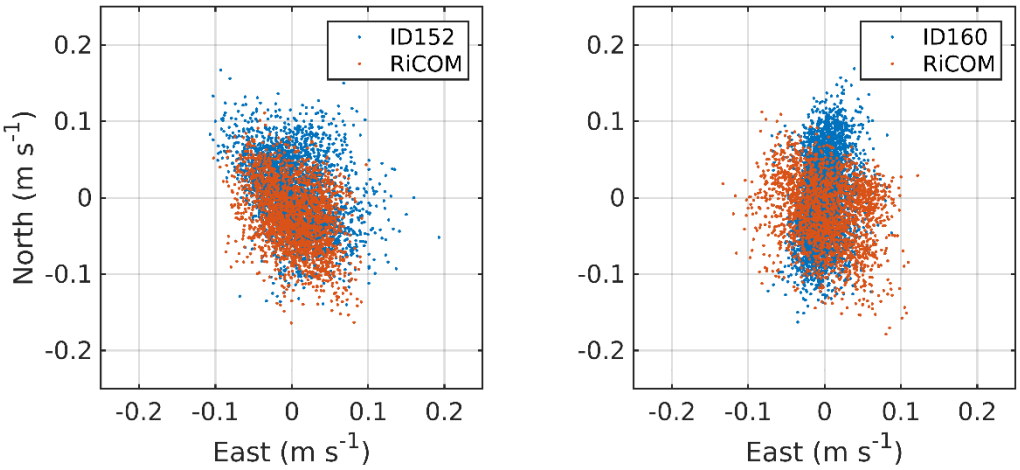

Figure 23. Modelled near-bed East and North components of velocity at the northern (left) and southern (right) ADCP locations for the period January – April 2020. The measured near-bed data from earlier ADCP deployments ID152 and ID160 are shown for indirect (not contemporaneous) comparison.

6. References

Casulli, V. 1987. Eulerian-lagrangian methods for hyperbolic and convection dominated parabolic problems. In: Taylor, C., Owen, D., Hinton, E. (Eds.), Computational Methods for Non-linear Problems, Pineridge Press, Swansea,U.K., pp. 239–268.

Elliott A.E., Gillibrand, P.A. and Turrell, W.R., 1992. Tidal mixing near the sill of a Scottish sea loch. In Dynamics and exchanges in estuaries and the coastal zone, Coastal and Estuarine Studies, 40, D. Prandle (ed.), American Geophysical Union, Washington D.C., pp 35 56.

ECMWF, 2021. ERA5 dataset. European Centre for Medium-Range Weather Forecasts (ECMWF), https://www.ecmwf.int/en/forecasts/datasets/reanalysis-datasets/era5

Gillibrand, P.A.; Lane, E.M.; Walters, R.A.; Gorman, R.M., 2011. Forecasting extreme sea surface height and coastal inundation from tides, surge and wave setup. Austr. J. Civil Eng. 9, 99-112.

Gillibrand, P.A., Walters, R.A., and McIlvenny, J., 2016. Numerical simulations of the effects of a tidal turbine array on near-bed velocity and local bed shear stress. *Energies*, vol 9, no. 10, pp. 852. DOI: 10.3390/en9100852

Lane, E.M.; Gillibrand, P.A.; Arnold, J.R.; Walters, R.A., 2011. Tsunami inundation modeling with RiCOM. Austr. J. Civil Eng., 9, 83-98.

Large. W.G. and Pond, S., 1981. Open ocean momentum flux measurements in moderate to strong winds. J. Phys. Oceanogr., 11, 324—336.

Marine Scotland, 2016. Wider Loch Linnhe System Climatology 1.02. Available at: https://marine.gov.scot/opendata/dataset/wider-loch-linnhe-system-climatology-102

Marine Scotland, 2016b. The wider domain Scottish Shelf Model, Marine Scotland, Available at: http://marine.gov.scot/information/wider-domain-scottish-shelf-model

McIlvenny, J. , Tamsett, D., Gillibrand, P.A. and Goddijn-Murphy, L., 2016. Sediment Dynamics in a Tidally Energetic Channel: The Inner Sound, Northern Scotland. Journal of Marine Science and Engineering, 4, 31; doi:10.3390/jmse4020031

Mowi, 2022. Macleans Nose Waste Solids Deposition Modelling Report. Mowi Scotland Ltd, May 2022, 19 pp.

Pawlowicz, R.; Beardsley, B.; Lentz, S. Classical tidal harmonic analysis including error estimates in MATLAB using T_TIDE. Computers & Geosciences. 2002, 28, 929-937.

Plew, D. R.; Stevens, C. L. 2013. Numerical modelling of the effect of turbines on currents in a tidal channel–Tory Channel, New Zealand. Renew. Energy, 57, 269-282.

UKHO 2022, https://www.admiralty.co.uk/digital-services/data-solutions/admiralty-marine-data-portal

Umlauf, L.; Burchard, H. 2003. A generic length-scale equation for geophysical turbulence models, J. Mar. Res., 61, 235-265.

Walters, R. A. 2005a. Coastal ocean models: two useful finite element methods. Cont. Shelf Res., 25(7), 775-793.

Walters, R. A. 2005b. A semi-implicit finite element model for non-hydrostatic (dispersive) surface waves. Int. J. Num. Meth. Fluids, 49(7), 721-737.

Walters, R.A. 2016. A coastal ocean model with subgrid approximation. *Ocean Mod*., 102, 45-54.

Walters, R.A.; Casulli, V., 1998. A robust, finite element model for hydrostatic surface water flows. Comm. Num. Methods Eng., 14, 931–940.

Walters, R.A.; Gillibrand, P.A.; Bell, R.; Lane, E.M. 2010. A Study of Tides and Currents in Cook Strait, New Zealand. Ocean Dyn., 60, 1559-1580.

Walters, R.A., Lane, E.M., Hanert, E. 2009. Useful time-stepping methods for the Coriolis term in a shallow water model. *Ocean Model*., *28*, 66–74. doi: 10.1016/j. ocemod.20 08.10.0 04.

Walters, R.A. ; Lane, E.M.; Henry, R.F. 2008. Semi-lagrangian methods for a finite element coastal ocean model. *Ocean Model*., 19, 112–124.

Walters, R. A.; Tarbotton, M. R.; Hiles, C. E. 2013. Estimation of tidal power potential. Renew. Energy, 51, 255-262.

Warner, J.C.; Sherwood, C.R.; Arango, H.G.; Signell, R.P.; 2005. Performance of four turbulence closure models implemented using a generic length scale method. Ocean Modelling, 8, 81 – 113.

Willmott, C. J.; Ackleson, S. G.; Davis, R. E.; Feddema, J. J.; Klink, K. M.; Legates, D. R. O'Donnell, J.; Rowe, C. M. 1985. Statistics for evaluation and comparison of models, J. Geophys. Res., 90, 8995– 9005.

Wu, J. 1982. Wind-stress coefficients over sea surface from breeze to hurricane, J. Geophys. Res., 87(C12), 9704–9706, doi:10.1029/JC087iC12p09704.